Dynamical mean-field theory for molecular electronics: Electronic structure and transport properties

D. Jacob,[1,2,][*] K. Haule,[3] and G. Kotliar[3]

[1]*Max-Planck-Institute für Mikrostrukturphysik, Weinberg 2, 06102 Halle, Germany*
[2]*European Theoretical Spectroscopy Facility (ETSF)*
[3]*Department of Physics & Astronomy, Rutgers University, 136 Frelinghuysen Road, Piscataway, New Jersey 08854, USA*

We present an approach for calculating the electronic structure and transport properties of nanoscopic conductors that takes into account the dynamical correlations of strongly interacting d or f electrons by combining density-functional theory calculations with the dynamical mean-field theory. While the density-functional calculation yields a static mean-field description of the weakly interacting electrons, the dynamical mean-field theory explicitly takes into account the dynamical correlations of the strongly interacting d or f electrons of transition metal atoms. As an example we calculate the electronic structure and conductance of Ni nanocontacts between Cu electrodes. We find that the dynamical correlations of the Ni $3d$ electrons give rise to quasiparticle resonances at the Fermi level in the spectral density. The quasiparticle resonances, in turn, lead to Fano line shapes in the conductance characteristics of the nanocontacts similar to those measured in recent experiments of magnetic nanocontacts.

PACS number(s): 73.63.Rt, 71.27.+a

I. INTRODUCTION

State of the art for calculating the conductance and current through atomic- and molecular-size conductors consists in combining *ab initio* electronic-structure calculations on the level of density-functional theory (DFT) with the Landauer formalism or nonequilibrium Green's function technique.[1,2] This methodology has been quite successful for the theoretical description of, e.g., metallic nanocontacts[3] predicting zero-bias conductances that are, in general, in good agreement with experiments even in the case of nanocontacts made from magnetic transition metals.[4–9]

Recently, however, nanocontacts made from Fe, Co, or Ni have been reported to display Kondo effect.[10,11] This has been inferred from the observation of Fano line shapes[12] in the low-voltage conductance characteristics similar to those observed in recent scanning tunnel microscope experiments with magnetic adatoms on metal surfaces.[13–16] The observation of the Kondo effect in Fe, Co, and Ni nanocontacts is rather surprising since these materials are strong ferromagnets as bulk materials. The Kondo effect, however, is usually at odds with ferromagnetism as it results from the screening of a local magnetic moment by antiferromagnetic coupling to the conduction electrons.[10,17]

DFT-based transport calculations of nanoscopic conductors cannot capture truly many-body effects as the Kondo effect that originate from the dynamic correlations of strongly interacting electrons. Therefore it is necessary to extend the existing methodology in order to account for dynamic electron correlations in transport experiments of nanoscopic conductors. Recent approaches to include dynamic electron correlations in the *ab initio* description of quantum transport are based on the GW approximation (GWA) (Ref. 18) or the three-body scattering (3BS) formalism.[19] While the GWA is only suitable for weakly correlated systems due to the perturbative treatment of the electron-electron interactions, the 3BS is, in principle, capable of describing more

strongly correlated systems as it goes beyond perturbation theory. However, the 3BS does not provide a satisfactory solution of the Anderson-impurity problem since the local correlations are not taken into account properly. More recently, *ab initio* electronic-structure methods on the level of DFT or the GW approximation have been combined with more sophisticated many-body techniques such as the one-crossing approximation (OCA) or the numerical renormalization group in order to account for the Kondo effect in nanoscopic systems containing single magnetic atoms.[20–23]

In this paper we develop an approach inspired by the success of the dynamical mean-field theory (DMFT) in the treatment of correlated solids,[24,25] to tackle the challenges of molecular electronics. DMFT is an approach based on the locality of the self-energy and does not require Bloch periodicity. It has been applied before to strongly spatially inhomogeneous systems such as alloys near an Anderson transition,[26] surfaces[27] and interfaces,[28] multilayered heterostructures,[29] and cold atoms in a trap.[30] Notice, however, that so far all these studies were restricted to *model Hamiltonians* as, for example, the Hubbard model.

In order to incorporate realistic aspects of the electronic structure we extend the DFT+DMFT philosophy[31,32] to the case of nanoscopic conductors. Our *molecular* DMFT approach takes into account the local dynamical correlations of the strongly interacting $3d$ or $4f$ shells of the magnetic atoms within a nanoscopic conductor such as a molecule or nanocontact which is coupled to semi-infinite electrodes while the rest of the system is treated on a static mean-field level by the local-density approximation (LDA). This approach can also be viewed as an extension of the early work of one of us[33] which ignored dynamical correlations of open atomic shells. In the limiting case where the correlated region reduces to a single atom, our approach reduces to our previous work which treated a single magnetic impurity in a metallic nanocontact.[20] When the device region contains several correlated atoms in close proximity, the molecular DMFT treat-
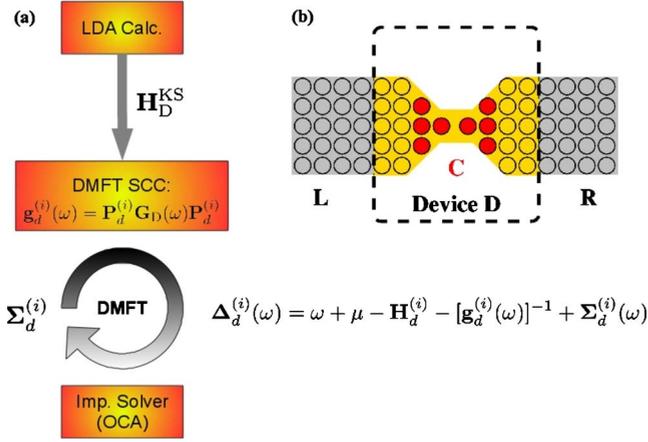
FIG. 1. (Color online) (a) Molecular DMFT self-consistency cycle applied to nanoscopic conductors. (b) Division of the system into left (L) and right (R) electrodes, and the central device region (D) that hosts the strongly correlated subspace (C) consisting of the strongly correlated d orbitals of the magnetic atoms shown as red (dark gray) circles.

ment is essential since the effective bath of each correlated atoms obeys a self-consistency condition which involves the whole device region.

Our work is similar in spirit to the recently presented dynamical vertex approximation for nanoscopic systems (nano-DΓA) by Valli *et al.*[34] This approach can, in principle, treat nonlocal self-energy effects. In a related work, Florens introduced a nano-DMFT approach whereby a correlated system is approximated by embedding it in a model geometry having a treelike structure.[35] However, both methods[34,35] have been implemented in the context of the Hubbard model while we demonstrate that the existing molecular DMFT technology can treat a realistic nanocontact.

This paper is organized as follows. In Sec. II we describe the molecular DMFT method for nanoscopic conductors. In Sec. III we apply the method to small Ni nanocontacts connected to Cu nanowires and discuss the results. Finally, we conclude this paper with a general discussion of the method and of the results in Sec. IV.

II. METHOD

We consider a nanoscopic conductor bridging two semi-infinite metal wires as shown schematically in Fig. 1(b). As indicated, the nanoscopic conductor contains magnetic atoms that give rise to dynamic electron correlations due to the strongly interacting $3d$ electrons. The nanoscopic conductor could be, for example, a molecule, a nanowire, a nanocluster, or simply an atomic-size constriction in the metal wire.

In order to describe the dynamic correlations that arise from the $3d$ shells of the magnetic atoms we adapt the LDA+DMFT method to the case of nanoscopic conductors. To this end it is convenient to divide the system into three parts as shown in the upper right panel of Fig. 1. Two semi-infinite metallic leads L and R, and the central device region (D) which contains the nanoscopic conductor and the magnetic atoms with the strongly interacting $3d$ shells, as well as

a sufficient part of the two metallic leads so that the electronic structure of the leads has relaxed to that of bulk (i.e., infinite) electrodes. The correlated subspace (C) that will be described on the level of DMFT is thus given by the direct sum of the $3d$ subspaces of all magnetic atoms (M) in the device region.

The effective one-body Hamiltonians of the device region and leads are obtained from DFT calculations on the level of LDA. Here we use the supercell approach (see Appendix A) to obtain the effective Kohn-Sham (KS) Hamiltonians of each part of the system prior to the dynamical treatment of the impurity d shell and the transport calculations. The electronic structure of the device region is calculated with the CRYSTAL06 *ab initio* electronic-structure program for periodic systems[36] by defining a one-dimensional periodic system consisting of the device region as the unit cell.

The device Hamiltonian $\mathbf{H}_\mathrm{D}$ is then obtained from the converged KS Hamiltonian of the unit cell of the periodic system. In the same way, the unit-cell Hamiltonians $\mathbf{H}^0_\mathrm{L/R}$ and hoppings $\mathbf{V}_\mathrm{L/R}$ between unit cells of the left and right leads can be extracted from calculations of infinite nanowires with finite width since the electronic structure in the semi-infinite leads has relaxed to that of an infinite nanowire.

The strong electron correlations of the $3d$ shells of the magnetic atoms are captured by adding a Hubbard-type interaction term to the one-body Hamiltonian within the correlated subspace d of each of the magnetic atoms i

$$\hat{\mathcal{H}}^{(i)}_U = \frac{1}{2} \sum_{\substack{\alpha_1,\beta_1,\alpha_2,\beta_2 \\ \sigma_1,\sigma_2}} U^{(i)}_{\alpha_1\alpha_2\beta_1\beta_2} \hat{d}^\dagger_{i\alpha_1\sigma_1} \hat{d}^\dagger_{i\alpha_2\sigma_2} \hat{d}_{i\beta_2\sigma_2} \hat{d}_{i\beta_1\sigma_1}, \quad (1)$$

where $\hat{d}^\dagger_{i\alpha\sigma}(\hat{d}_{i\alpha\sigma})$ creates (annihilates) an electron with spin σ in the $3d$ orbital α on atom i. $U^{(i)}_{\alpha_1\alpha_2\beta_1\beta_2}$ are the matrix elements of the effective (i.e., screened) Coulomb interaction of the $3d$ electrons which is smaller than the bare Coulomb interaction due to the screening by the conduction electrons. Here we take a model interaction taking into account only the direct Coulomb repulsion U between electrons (i.e., $U_{\alpha\beta\alpha\beta} \equiv U$) and the Hund's rule coupling J (i.e., $U_{\alpha\beta\beta\alpha} \equiv J$ for $\alpha \neq \beta$). For $3d$ transition-metal elements in bulk materials the repulsion U is typically around 2–3 eV and J is around 0.9 eV.[37] However, due to the lower coordination of the atoms in the contact region or molecule the screening of the direct interaction should be somewhat reduced compared to bulk. Here we take $U=5$ eV and $J=0.9$ eV as in our previous work.[20]

The Coulomb interaction within the correlated $3d$ subspaces of the magnetic atoms has already been taken into account on a static mean-field level in the effective KS Hamiltonian of the device. Therefore the KS Hamiltonian within each $3d$ subspace has to be corrected by a double-counting correction term, i.e., $\mathbf{H}^{(i)}_d \equiv \mathbf{P}^{(i)}_d \mathbf{H}^{KS}_\mathrm{D} \mathbf{P}^{(i)}_d - \mathbf{H}^{(i)}_\mathrm{dc}$, where $\mathbf{P}^{(i)}_d$ is the projection onto the $3d$ subspace of atom i.[38] Here we use the standard expression[39]

$$\mathbf{H}^{(i)}_\mathrm{dc} = \left[U\left(N^{(i)}_d - \frac{1}{2}\right) - \frac{1}{2}J(N^{(i)}_d - 1) \right] \times \mathbf{P}^{(i)}_d \quad (2)$$

where $N^{(i)}_d$ is the occupation of the $3d$ shell of atom i.

The central quantity is the Green's function of the device region

$$\mathbf{G}_D = [(\omega + \mu)\mathbf{S}_D - \mathbf{H}_D + \mathbf{H}_{dc} - \mathbf{\Sigma}_C - \mathbf{\Sigma}_L - \mathbf{\Sigma}_R]^{-1}, \quad (3)$$

where $\mathbf{\Sigma}_C$ is the electronic self-energy that describes the dynamic electron correlations of the electrons within the correlated subspace C and $\mathbf{H}_{dc}$ is the double-counting correction within the entire correlated subspace C, i.e., $\mathbf{H}_{dc} \equiv \Sigma_{i \in M} \mathbf{H}_{dc}^{(i)}$. $\mathbf{S}_D$ is the overlap matrix taking into account the nonorthogonality of basis set.[40] μ is the chemical potential, $\mathbf{\Sigma}_L$ and $\mathbf{\Sigma}_R$ are the so-called lead self-energies[41] which describe the coupling of the device to the semi-infinite leads L and R, respectively. These can be calculated from the effective one-body Hamiltonians of the leads by iteratively solving the Dyson equation for the lead self-energies, Eq. (A1).

The central assumption of DMFT is that the intersite correlations, i.e., the correlations between electrons located on different atoms can be neglected. In that case the electron-correlation self-energy $\mathbf{\Sigma}_C$ becomes block diagonal, and each block corresponds to the self-energy $\mathbf{\Sigma}_d^{(i)}$ of the correlated $3d$ subspace of a magnetic atom i: $\mathbf{\Sigma}_d^{(i)} = \mathbf{P}_d^{(i)} \mathbf{\Sigma}_C \mathbf{P}_d^{(i)}$. The self-energies $\mathbf{\Sigma}_d^{(i)}$ and hence the overall self-energy $\mathbf{\Sigma}_C$ can now be determined by mapping onto a generalized Anderson-impurity problem for each correlated subspace, described by the following Green's function:

$$\mathbf{g}_d^{(i)}(\omega) = [\omega + \mu - \mathbf{H}_d^{(i)} - \mathbf{\Sigma}_d^{(i)}(\omega) - \mathbf{\Delta}_d^{(i)}(\omega)]^{-1}, \quad (4)$$

where we have introduced the so-called hybridization function $\mathbf{\Delta}_d^{(i)}$ which describes the coupling of the correlated subspace with the rest of the system. The hybridization function is determined by the DMFT self-consistency condition:

$$\mathbf{g}_d^{(i)}(\omega) = \mathbf{P}_d^{(i)} \mathbf{G}_D(\omega) \mathbf{P}_d^{(i)}. \quad (5)$$

It follows that the hybridization function is given by

$$\mathbf{\Delta}_d^{(i)}(\omega) = \omega + \mu - \mathbf{H}_d^{(i)} - [\mathbf{g}_d^{(i)}(\omega)]^{-1} - \mathbf{\Sigma}_d^{(i)}(\omega). \quad (6)$$

The Eqs. (3)–(6) define the molecular DMFT self-consistency cycle for the calculation of the self-energies $\mathbf{\Sigma}_d^{(i)}$. One starts with the effective one-body Hamiltonian $\mathbf{H}_D$ obtained from the LDA calculation and an initial guess for the local correlation self-energies $\mathbf{\Sigma}_d^{(i)}$ (usually zero). This allows one to calculate the device Green's function, Eq. (3), and consequently the projection $\mathbf{g}_d^{(i)}$. Thus one obtains the Hybridization functions $\mathbf{\Delta}_d^{(i)}(\omega)$ which together with the on-site energy levels $\mathbf{H}_d^{(i)}$ and the Coulomb interaction U, J defines the Anderson-impurity problem which can be solved by an impurity solver, and one obtains a new self-energy $\mathbf{\Sigma}_d^{(i)}$. The DMFT self-consistency cycle is illustrated in Fig. 1(a).

Solving the generalized Anderson-impurity problem is a difficult task, and at present there is no universal impurity solver that works efficiently and accurately in all parameter regimes. Here we make use of impurity solvers based on an expansion in the hybridization strength given by $\Delta_d^{(i)}(\omega)$ around the atomic limit. The starting point is an exact diagonalization of the (isolated) impurity subspace, i.e., the $3d$ shell of the magnetic atom given by the interacting Hamil-

tonian $\hat{\mathcal{H}}_d^{(i)} + \hat{\mathcal{H}}_U^{(i)}$. The hybridization of the impurity subspace with the rest of the system [given by the hybridization function $\Delta_d^{(i)}(\omega)$] is then treated perturbatively.

The so-called noncrossing approximation[42] (NCA) is a self-consistent perturbation expansion to lowest order in the hybridization strength. NCA only takes into account bubble diagrams describing hopping processes where an electron or hole hops into the impurity at some time and then out at a later time (see Fig. 9 in Appendix B). The OCA (Refs. 43 and 44) improves on the NCA by taking into account second-order diagrams where two additional electrons (holes) are accommodated on the impurity at the same time as shown in Fig. 9. OCA improves considerably many of the shortcomings of NCA.[42] It substantially improves the width of the Kondo peak and hence the Kondo temperature which now are only slightly underestimated. It also corrects the asymmetry of the Kondo peak. For very low temperatures ($T \ll T_K$), however, the height of the Kondo peak is still overestimated, and the Fermi-liquid behavior at zero temperature is not recovered.[44]

Hence, OCA is a reasonable approximation for solving the generalized impurity problem as long as the temperatures are not too low (i.e., more than one order of magnitude below T_K). In Appendix B we give a brief introduction to the NCA and OCA impurity solvers. A detailed description of the NCA and OCA methods can be found, e.g., in Refs. 17, 31, and 42–45.

The current through a strongly interacting region can be calculated exactly by the Meir-Wingreen formula.[46] But in order to apply the Meir-Wingreen result one has to solve the impurity problem out of equilibrium which is a difficult task that has only been accomplished very recently and only in the context of model Hamiltonians.[47,48] However, Meir and Wingreen also showed that for low temperatures and small bias voltages the Meir-Wingreen expression is well approximated by the much simpler Landauer formula[49]

$$I(V) = \frac{2e}{h} \int_0^{eV} d\omega T(\omega), \quad (7)$$

where $T(\omega)$ is the Landauer transmission function and where we have assumed an asymmetric voltage drop V about the device region. Thus the conductance is simply given by the Landauer transmission function

$$\mathcal{G}(V) = \frac{\partial I}{\partial V}(V) = \frac{2e^2}{h} T(eV). \quad (8)$$

The latter can be calculated from the (equilibrium) device Green's function

$$T(\omega) = \text{Tr}[\mathbf{\Gamma}_L(\omega)\mathbf{G}_D^\dagger(\omega)\mathbf{\Gamma}_R(\omega)\mathbf{G}_D(\omega)], \quad (9)$$

where $\mathbf{\Gamma}_{L/R}$ are the so-called coupling matrices which describe the coupling to the leads and can be calculated from the lead self-energies by $\mathbf{\Gamma}_{L/R} = i(\mathbf{\Sigma}_{L/R} - \mathbf{\Sigma}_{L/R}^\dagger)$.

III. RESULTS AND DISCUSSION

In the following we demonstrate the above developed molecular DMFT method for the two idealized Ni nanocontacts
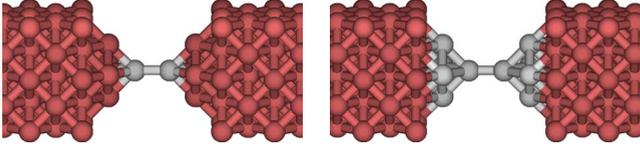
FIG. 2. (Color online) (a) Ni dimer between the tips of two Cu nanowires grown in the 001 direction of bulk Cu. (b) Ni nanocontact consisting of ten atoms between two Cu 001 nanowires. Ni atoms are shown in light gray (light gray) and Cu atoms are shown in red (dark gray).

with Cu nanowires as electrodes shown in Fig. 2. Ni nanocontacts have been a subject of intense research in the last decade as prospective ingredients for nanoscale spintronics devices.[4–9,50,51] Here we consider the paramagnetic phase, i.e., the self-energies and the Green's functions are spin degenerate. Breaking of the spin symmetry by an external magnetic field or by spin-polarized electrodes is not taken into account.

A. Ni dimer between Cu nanowires

First, we consider a dimer of Ni atoms between two semi-infinite Cu nanowire electrodes as shown in Fig. 2(a). The nanowires are grown in the 001 direction of bulk Cu. The distance between the two Ni tip atoms is 2.4 Å, all other distances are those of bulk Cu. For the sake of simplicity, we have not relaxed the atomic positions. Due to the highly idealized geometry both Ni atoms are equivalent. Hence in each step of the molecular DMFT self-consistency we only have to solve the impurity problem once.

In spite of the highly symmetric situation the Ni $3d$ orbitals split into four different symmetry groups. As can be seen from Fig. 3(a) which shows the hybridization function in the first step of the self-consistent DMFT procedure [where the self-energy $\Sigma_d(\omega)$ is zero], the hybridization functions are quite different for each of the four symmetry groups. This situation is different from that of the corresponding bulk systems where the hybridization functions for each correlated orbital are usually very similar due to the highly isotropic closed-packed crystal structures. In the geometry considered here, the doubly degenerate $3d_{xz}$ and $3d_{yz}$ orbitals have the strongest hybridization around the Fermi level with the rest of the system. Also the $3d_{3z^2-r^2}$ orbital has an appreciable hybridization. The hybridization of the $3d_{xy}$ and $3d_{x^2-y^2}$ orbitals on the other hand are smaller by at least one order of magnitude.

Figure 3(b) shows the hybridization function after self-consistency has been reached in the DMFT calculation. Now the converged self-energy $\Sigma_d(\omega)$ is nonzero in general. We can see that the DMFT self-consistency has a considerable effect on the hybridization function for most of the Ni $3d$ orbitals. For example, the hybridization of the degenerate $3d_{xz}$ and $3d_{yz}$ orbitals around the Fermi level is strongly increased. Moreover a sharp peak appears right at the Fermi level. Additional features also arise in the hybridization functions of the other $3d$ orbitals. The additional features in the $3d$-hybridization functions of one Ni atom stem from the corresponding features (induced by the on-site interactions)
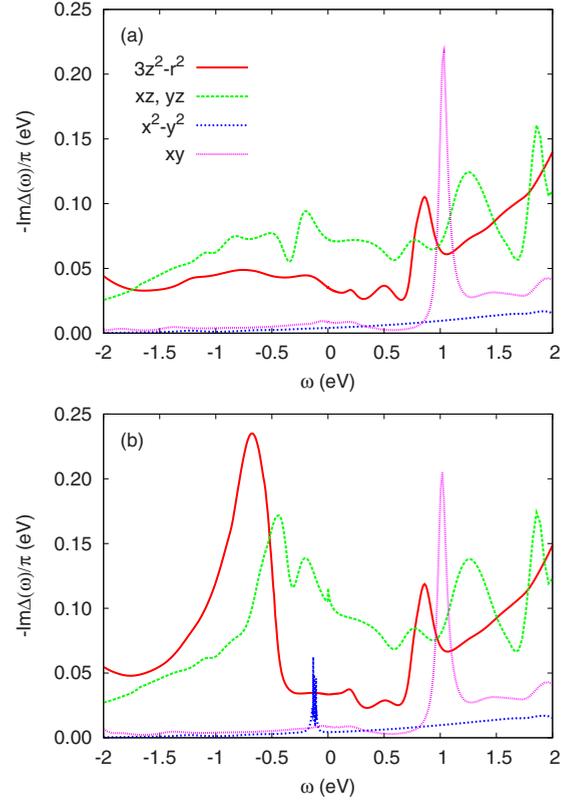
FIG. 3. (Color online) Imaginary part of hybridization functions for different Ni $3d$ orbitals in the dimer geometry shown in Fig. 2(a), (a) in the first step and (b) in the last step of the self-consistent molecular DMFT calculation at low temperature ($T=12$ K).

in the $3d$-spectral density of the other Ni atom.

In Fig. 4 we show the temperature dependence of the Ni $3d$ spectrum calculated with molecular DMFT and compare them to the spectrum calculated with LSDA. The DMFT spectra are somewhat smother than the LSDA spectra due to the finite lifetime broadening of the single-particle states by the electron-electron interactions. Most importantly, the molecular DMFT spectrum shows a strong temperature dependence which cannot be captured by a static mean-field
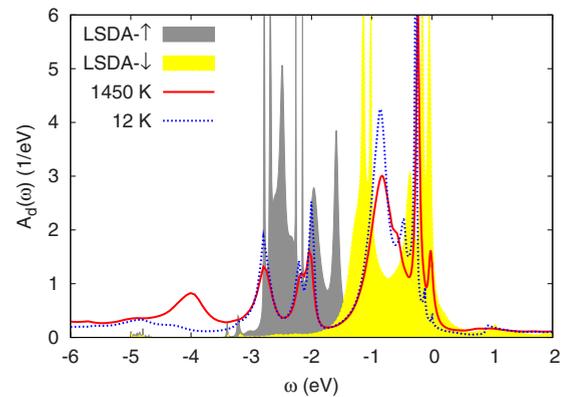
FIG. 4. (Color online) Ni $3d$-spectral function for the Ni dimer between Cu nanowires shown in Fig. 2(a) calculated with molecular DMFT at two different temperatures on one hand and calculated with LSDA on the other hand.
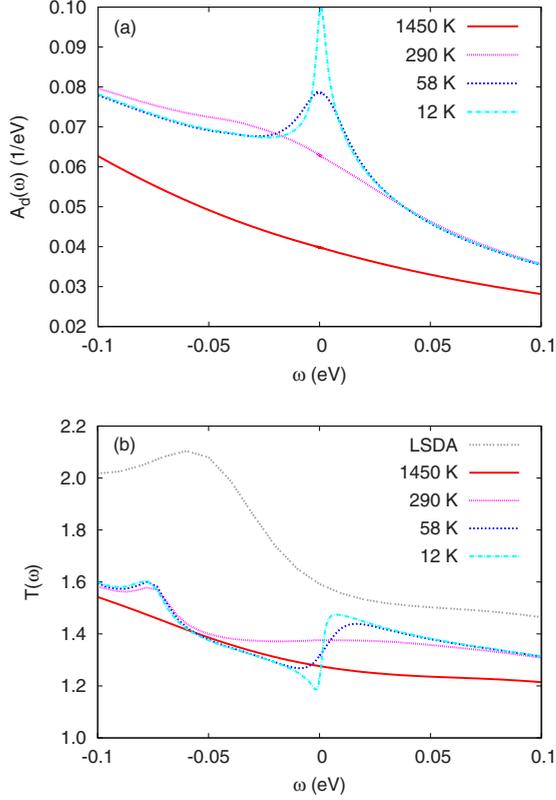
FIG. 5. (Color online) (a) Spectral function of Ni $3d_{xz}$ and $3d_{yz}$ orbitals near the Fermi level for different temperatures. (b) Correlated transmission function calculated with molecular DMFT at different temperatures compared to LSDA transmission function near the Fermi level.

treatment like LSDA. For example, at low temperatures a small peak forms right at the Fermi level in the molecular DMFT spectrum. This is a quasiparticle peak that originates from the two degenerate $3d_{xz}$ and $3d_{yz}$ orbitals as can be seen from Fig. 5(a). Strictly speaking, it is not a Kondo peak since the occupation of the two orbitals is around 3.65 and hence these orbitals are in the so-called mixed-valence regime where in addition to the spin fluctuations also charge fluctuations take place (see, e.g., the book by Hewson[17] for a detailed discussion). However, we would like to emphasize here that the corresponding magnetic moment is nevertheless screened by the conduction electrons.

We can find the weight Z and the linewidth Γ of the quasiparticle by fitting the peak to a Lorentzian. Figure 5(a) suggests that the $3d_{xz}$, $3d_{yz}$ spectral functions near the Fermi level can be fitted to a weighted Lorentzian plus a linear function

$$A_d(\omega) = a\omega + b + \frac{Z}{\pi} \frac{\Gamma/2}{\omega^2 + \Gamma^2/4}. \tag{10}$$

We find a very tiny quasiparticle weight Z of less than 0.1% and a width Γ corresponding to a temperature of about 130 K. This is the critical temperature below which the quasiparticle can be observed (and which in the case of Kondo effect is called Kondo temperature). Note that the width of the

TABLE I. Orbital occupations n_d (at low temperature) and effective energy levels $\tilde{\epsilon}_d \equiv \epsilon_d + \mathrm{Re}\,\Delta_d(0)$ of the $3d$ orbitals of the Ni tip atoms in the case of the Ni dimer geometry and the Ni nanocontact consisting of ten Ni atoms. ϵ_d denotes the KS energy levels before double-counting correction.

	Ni dimer		Ni_{10} nanocontact	
	n_d	$\tilde{\epsilon}_d$ (eV)	n_d	$\tilde{\epsilon}_d$ (eV)
$3z^2 - r^2$	1.8801	−5.2188	1.9336	−5.4886
xz, yz	3.6468	−5.1296	3.7395	−5.3954
$x^2 - y^2$	1.9174	−4.8121	1.0096	−5.1749
xy	0.9943	−4.7410	1.9578	−5.2706

quasiparticle is somewhat enhanced by the DMFT self-consistency compared to the case without DMFT (not shown).

The quasiparticle peak leads to a corresponding Fano feature in the transmission function as can be seen in Fig. 5(b) which shows the transmission function for small energies around the Fermi level. Hence our calculations show that the low-bias conductance of the Ni dimer between Cu electrodes features a Fano line shape due to a quasiparticle peak in the Ni $3d$ spectral function at low temperatures.

Table I lists the individual occupations of all Ni $3d$ orbitals and the corresponding effective energy levels that are obtained from the KS energy levels plus the real part of the hybridization function at zero frequency. We can see that all orbitals apart from the d_{xy} orbital have mixed valences and are almost full. The d_{xy} orbital on the other hand is basically half filled. Hence this orbital would be a candidate for a true Kondo effect, i.e., screening of the magnetic moment by spin fluctuations only. However, the hybridization of this orbital is very low, as can be seen from Fig. 3. Hence the Kondo temperature for this orbital is very low so that the orbital does not enter the Kondo regime at the temperatures considered here but is in the local moment regime.

B. Ni nanocontact between Cu electrodes

Now we turn to the slightly more complicated case of the Ni nanocontact consisting of ten atoms between two Cu nanowires as shown in Fig. 2(b). As before the nanowires are grown in the 001 direction of bulk Cu. The distance between the two Ni tip atoms is 2.4 Å while all other distances are those of bulk Cu. As before the two Ni tip atoms are both equivalent. On the other hand, the eight outer atoms of the Ni nanocontact are not equivalent with the tip atoms but are equivalent among themselves. Hence we have to solve two different impurity problems in each step of the molecular DMFT self-consistency cycle.

In Fig. 6, we show the $3d$ spectral function of (a) the base atoms and (b) the tip atoms of the Ni nanocontact calculated on one hand with molecular DMFT at different temperatures and on the other hand with DFT on the level of the LDA. We see that in both cases the molecular DMFT spectral densities are quite different from the LSDA ones. Both LSDA spectra
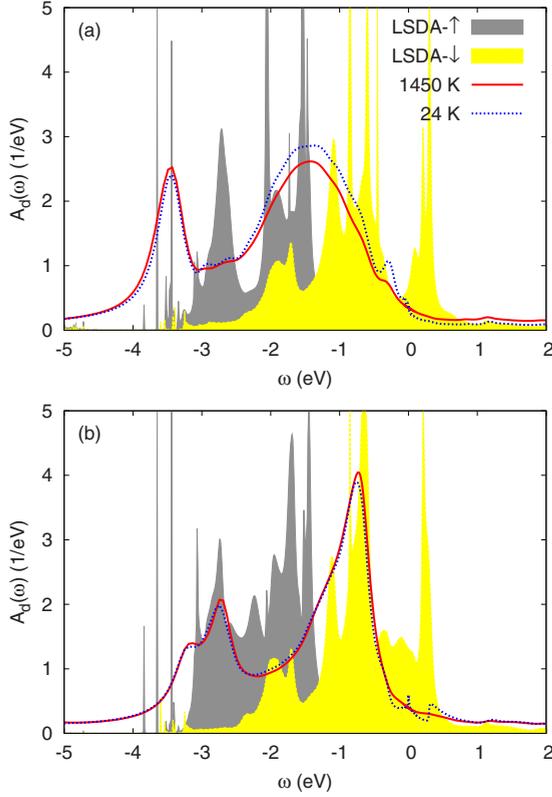
FIG. 6. (Color online) (a) $3d$-spectral function of a Ni atom at the base of one of the pyramids of the Ni nanocontact between Cu nanowires shown in Fig. 2(b) calculated on one hand with molecular DMFT at two different temperatures and with LSDA on the other hand. (b) Same as (a) but for the tip atoms of the Ni nanocontact.

FIG. 7. (Color online) (a) Spectral function of $3d_{xz}$ and $3d_{yz}$ orbitals of Ni tip atoms near the Fermi level for different temperatures. (b) Correlated transmission function at different temperatures compared to LSDA transmission function for energies around the Fermi level.

feature a strong peak above the Fermi level for the minority electrons that is absent in the molecular DMFT spectra. Moreover, near the Fermi level, the molecular DMFT spectrum of the tip atoms is strongly temperature dependent due to the formation of a quasiparticle peak at the Fermi level in the degenerate $3d_{xz}$ and $3d_{yz}$ levels for low temperatures. Figure 7(a) shows a closeup of the formation of the quasiparticle peak in the spectral density of the $3d_{xz}$ and $3d_{yz}$ levels. Fitting to a Lorentzian plus linear function, Eq. (10), we now find a slightly increased quasiparticle weight Z of 0.2% and also a somewhat increased width Γ corresponding to a critical temperature of 220 K as compared to the case of the Ni dimer. The increased width Γ and quasiparticle weight Z is due to the increased imaginary part of the hybridization function (not shown) of the tip atoms near the Fermi level which stems from the $3d$ spectral density of the base atoms of the Ni pyramid. In the dimer case, the base atoms of the pyramids are Cu atoms where the $3d$ spectral density near the Fermi level is negligible.

The occupation of the degenerate $3d_{xz}$ and $3d_{yz}$ orbitals is 3.73. Hence these orbitals are in the mixed-valence regime rather than the Kondo regime as in the case of the Ni dimer. Therefore the quasiparticle peak is strictly speaking not a Kondo peak. However, as was said before, the magnetic moment of these orbitals is nevertheless screened in the mixed-valence regime by the spin and charge fluctuations.

Figure 7(b) shows the transmission function near the Fermi level calculated on one hand with the molecular DMFT method at different temperatures and on the other and with DFT on the level of the LDA. As in the case of the dimer, the formation of the quasiparticle peak in the $3d_{xz}$ and $3d_{yz}$ orbitals at low temperatures leads to a temperature-dependent Fano line shape in the molecular DMFT transmission function. The LSDA transmission function on the other hand does not show such a behavior. On the contrary, it is rather flat and featureless at this energy scale. Also note that the LSDA transmission is considerably higher than the correlated transmission calculated with molecular DMFT. This is due to the correlations shifting a considerable part of the spectral weight of the $3d$ orbitals away from the Fermi level. Consequently, the overall contribution of the $3d$ orbitals to the transmission is higher in the case of the LSDA calculation than in the molecular DMFT calculation.

The transmission as calculated with the molecular DMFT approach, although lower than the LSDA one, is still compatible with the broad peak roughly between 1 and 1.7 $\times G_0$ in the experimentally measured conductance histograms of Ni nanocontacts.[5]

In Table I the orbital occupations and effective energy levels of individual Ni $3d$ orbitals of a tip atom of the Ni nanocontact are shown. The most striking difference with the Ni dimer (shown in the same table) is that now the $d_{x^2-y^2}$

orbital is the highest energy orbital with half filling instead of the d_{xy} orbital. This is a consequence of the different environment of the tip atom in the ten-atom nanocontact geometry compared to the dimer geometry. The presence of the $3d$ orbitals of the Ni atoms at the base of each pyramid near the Fermi levels change the hybridization functions of the tip atoms accordingly. Note that here the DMFT self-consistency is essential since without the self-consistency the hybridization functions would be very similar to the dimer case.

IV. SUMMARY AND CONCLUSIONS

We have developed a method for calculating the electronic structure and transport properties of nanoscopic conductors that explicitly takes into account local dynamical correlations originating from strong electron-electron interactions. Our method extends the established DFT-based *ab initio* transport methodology for nanoscopic conductors to include dynamic electron correlations originating from the strongly interacting $3d$ electrons of the transition-metal atoms. This is achieved by combining the DFT electronic-structure calculations of the nanoscopic conductor with a DMFT description of the strongly interacting $3d$ electrons in the device region. We thus obtain the correlated Green's function of the nanoscopic conductor which allows to calculate the electronic structure and the corresponding conductance in the low-bias voltage regime.

We have demonstrated the method for two model systems, namely, Ni nanocontacts consisting of several atoms and connected to Cu leads. We find that the dynamic correlations of the strongly interacting Ni $3d$ electrons give rise to strongly temperature-dependent spectra due to the formation of a quasiparticle peak at low temperatures. The quasiparticle peak gives rise to a temperature-dependent Fano-type line shape in the low-bias conductance characteristics similar to those measured in recent experiments with ferromagnetic nanocontacts.[11] Moreover, the critical temperatures of 120 and 220 K for the formation of the quasiparticle peak is in quite good agreement with the broad distribution of Kondo temperatures around the average temperature of 250 K extracted from the Fano line shapes in the low-bias conductance measurements of Ni nanocontacts in that same experiment. Note that a quasiparticle peak at the Fermi level can, in principle, also be obtained in the GW approximation.[52] However, in order to capture the quasiatomic features characteristic of the strong-correlation regime such as Hubbard bands or satellites together with the concomitant renormalization of the quasiparticle, a nonperturbative treatment of the local part of the Coulomb interaction such as the molecular DMFT method presented here is necessary.

The quasiparticle peak obtained here, is strictly speaking, not a Kondo peak since the system is in the so-called mixed-valence regime where charge fluctuations take place in addition to the spin fluctuations that lead to the Kondo effect. This hints at the possibility that the origin of the Fano line shapes in the low-bias conductance of Ni nanocontacts measured experimentally need not always be the Kondo effect. However, we would like to stress that also in the mixed-valence regime the magnetic moment of the corresponding orbitals would be screened. But to draw further conclusions in that matter, more realistic calculations are necessary taking into account the ferromagnetic leads and sampling over different contact geometries.

We have illustrated the molecular DMFT method for the case of simple nanocontacts containing several transition-metal atoms but the molecular DMFT approach is very general and can be applied to many systems of great theoretical and practical interest. For example, it can be used to treat large molecules in which one can isolate small clusters of correlated elements as, for example, in the fuel-cell materials of Tard *et al.*[53]

The molecular DMFT method allows to explicitly incorporate strong-dynamical correlations within the established DFT-based transport methodology for nanoscopic conductors. Our calculations show that dynamical correlations originating from the strongly interacting shells of magnetic atoms can alter the electronic structure and transport properties of nanoscopic conductors significantly.

APPENDIX A: DETAILS OF THE SUPERCELL APPROACH

In order to generate the effective one-body Hamiltonians of the device and leads the supercell approach is used. The electronic structure of the device region is calculated with the CRYSTAL06 *ab initio*[36] electronic-structure program for periodic systems by defining a one-dimensional periodic system consisting of the device region as the unit cell, as shown in Fig. 8(a). It is crucial that the device part D contains a sufficient part of the nanowire electrodes so that the two leads L and R are far enough away from the scattering region, and the electronic structure in the leads has relaxed to that of a bulk (i.e., infinite) nanowire. In that case the electronic structure of the periodic system build from a periodic repetition of the device region is the same as the electronic structure of the device between two semi-infinite nanowires as can be seen from Fig. 8. Thus the device Hamiltonian $\mathbf{H}_D$ can be obtained from the converged KS Hamiltonian of the unit cell of the periodic system.

In the same way the unit-cell Hamiltonians $\mathbf{H}_{L/R}^0$ and hoppings $\mathbf{V}_{L/R}$ between unit cells of the left and right leads are extracted from periodic calculations of infinite nanowires of finite width [see Figs. 8(b) and 8(c)]. Again it is crucial that the device region contains enough bulk electrode material so that the electronic structure in the electrodes is that of bulk
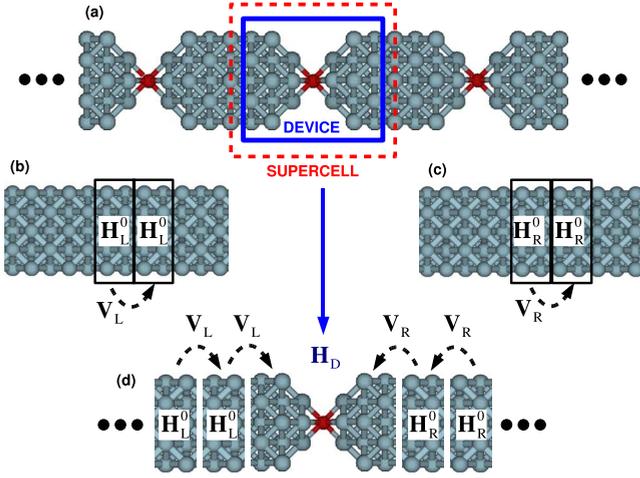
FIG. 8. (Color online) Illustration of the supercell approach to calculate the electronic structure of the device and of the leads. (a) One-dimensional periodic system to calculate the electronic structure of the device region. [(b) and (c)] Infinite nanowires to calculate the electronic structure of the left (L) and right (R) semi-infinite leads. (d) Sketch of the setup of the physical system. The device region (D) is suspended between two semi-infinite leads L and R.

nanowires. The lead self-energies $\boldsymbol{\Sigma}_L$, $\boldsymbol{\Sigma}_R$ which describe the coupling of the device region D to the semi-infinite nanowires L and R in the situation depicted in Fig. 8(d) can now be calculated by the following Dyson equation:

$$\boldsymbol{\Sigma}_{L/R}(\omega) = (\mathbf{V}_{L/R} - \omega\mathbf{S}_{L/R}) \times [\omega\mathbf{S}_{L/R}^0 - \mathbf{H}_{L/R}^0 - \boldsymbol{\Sigma}_{L/R}(\omega)]^{-1}(\mathbf{V}_{L/R}^\dagger - \omega\mathbf{S}_{L/R}^\dagger), \quad \text{(A1)}$$

where $\mathbf{S}_{L/R}^0$ and $\mathbf{S}_{L/R}$ are the overlap matrices taking into account the nonorthogonality of the basis set within the unit cell and between unit cells, respectively.

By this procedure we have connected the device region D with two *semi-infinite* nanowires that have the electronic structure of bulk, i.e., *infinite* nanowires. The supercell approach and the so-called partitioning technique used here to obtain the Green's function of a part of a system are discussed in more detail in the literature (see, e.g., Refs. 1, 2, 33, and 54).

APPENDIX B: THE NCA AND OCA IMPURITY SOLVERS

The general multiorbital Anderson-impurity model can be written in the following form:

$$\hat{\mathcal{H}} = \sum_{\alpha\beta} \epsilon_\alpha \hat{d}_\alpha^\dagger \hat{d}_\alpha + \frac{1}{2} \sum_{\alpha\beta\gamma\delta} U_{\alpha\beta\gamma\delta} \hat{d}_\alpha^\dagger \hat{d}_\beta^\dagger \hat{d}_\gamma \hat{d}_\delta + \sum_{k\nu\alpha} (V_{k\nu\alpha} \hat{c}_{k\nu}^\dagger \hat{d}_\alpha + V_{k\nu\alpha}^* \hat{d}_\alpha^\dagger \hat{c}_{k\nu}) + \sum_{k\nu} \epsilon_{k\nu} \hat{c}_{k\nu}^\dagger \hat{c}_{k\nu}, \quad \text{(B1)}$$

where in order to keep the notation simple we have combined the spin and orbital degrees of freedom into one index for each impurity level α and each band ν.

The NCA and the OCA both solve the Anderson-impurity model by expansion in the hybridization strength around the atomic limit. The starting point is an exact diagonalization of
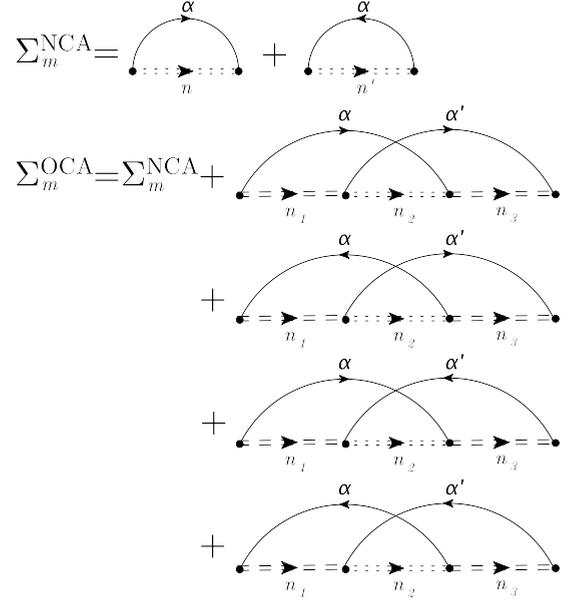
FIG. 9. Diagrams for pseudoparticle self-energies in the NCA (first row) and OCA (second and following rows) for some pseudoparticle m.

the impurity subspace (for example, the 3d shell of a magnetic atom) including the Hubbard-type interaction term

$$\hat{\mathcal{H}}_d \equiv \sum_{\alpha\beta} \epsilon_\alpha \hat{d}_\alpha^\dagger \hat{d}_\alpha + \frac{1}{2} \sum_{\alpha\beta\gamma\delta} U_{\alpha\beta\gamma\delta} \hat{d}_\alpha^\dagger \hat{d}_\beta^\dagger \hat{d}_\gamma \hat{d}_\delta \overset{\text{diag.}}{\rightarrow} \sum_m |m\rangle E_m \langle m|, \quad \text{(B2)}$$

where $|m\rangle$ are the many-body eigenstates of $\hat{\mathcal{H}}_d$ and E_m the respective eigenenergies.

One now introduces auxiliary fields $\hat{a}_m$, $\hat{a}_m^\dagger$ [called pseudoparticles (PPs)] such that each impurity state is represented by a corresponding pseudoparticle

$$\hat{a}_m^\dagger |\text{PPV}\rangle \equiv |m\rangle, \quad \text{(B3)}$$

where $|\text{PPV}\rangle$ is the pseudoparticle vacuum. The completeness of the impurity eigenstates imposes the following constraint:

$$Q \equiv \sum_m \hat{a}_m^\dagger \hat{a}_m = 1. \quad \text{(B4)}$$

The physical electron operators $\hat{d}_\alpha^\dagger$ can now be expressed by the PP operators:

$$\hat{d}_\alpha^\dagger = \sum_{n,m} (F^{\alpha\dagger})_{nm} \hat{a}_n^\dagger \hat{a}_m, \quad \text{(B5)}$$

where $(F^{\alpha\dagger})_{nm} \equiv \langle n|\hat{d}_\alpha^\dagger|m\rangle$ are the matrix elements of the impurity-electron creation operator. For later convenience we also define the corresponding matrix elements of the impurity-electron destruction operator as: $(F^\alpha)_{nm} \equiv \langle n|\hat{d}_\alpha|m\rangle$. The anticommutation rules for the physical electron operators then require that the PP $\hat{a}_m$ is a boson (fermion) if the corresponding state $|m\rangle$ contains an even (odd) number of electrons.

In the PP representation we can now rewrite the Hamiltonian of the generalized Anderson-impurity model as follows:

$$\hat{\mathcal{H}} = \sum_m E_m \hat{a}_m^\dagger \hat{a}_m + \sum_{k\nu} \epsilon_{k\nu} \hat{c}_{k\nu}^\dagger \hat{c}_{k\nu} + \lambda(Q-1)$$
$$+ \sum_{\substack{mn \\ k\nu\alpha}} [V_{k\nu,\alpha} \hat{c}_{k\nu}^\dagger \hat{a}_m^\dagger (F^\alpha)_{nm} \hat{a}_n + \text{H.c.}], \qquad (B6)$$

where we have included the constraint $Q \equiv 1$ into the Hamiltonian. The corresponding Lagrange multiplier λ can be interpreted as a (negative) chemical potential for the PPs.

In the PP picture, the hybridization with the bath electrons given by the last term in Eq. (B6) becomes now the interaction for the PPs. Because of the fermionic and bosonic commutation rules for the PPs, one can now develop a diagrammatic perturbation expansion in the PP interaction. The PP propagators can be written as

$$G_m(\omega) = [\omega - \lambda - E_m - \Sigma_m(\omega)]^{-1}, \qquad (B7)$$

where Σ_m is the PP self-energy describing the dynamic interaction of the PP m with the other PPs.

The NCA consists in taking into account the diagrams shown in the first row of Fig. 9 for some PP m. The NCA diagrams describe processes where a single electron (hole) jumps from the bath to the impurity and back thereby temporarily creating a PP with N+1 (N−1) electrons. The NCA equations correspond to a self-consistent perturbation expansion to lowest order in the hybridization function $\Delta_\alpha(\omega) \equiv \Sigma_{k,\nu} V_{k\nu,\alpha}^* V_{k\nu,\alpha}$. Since the fermionic self-energies depend on the dressed bosonic propagators, and vice versa, the NCA equations have to be solved self-consistently. Once the NCA equations are solved the physical quantities can be calculated from the PP self-energies.

The OCA takes into account second-order diagrams where two bath electron lines cross as shown in the last four rows of Fig. 9. The self-energies for the PPs again depend on the full propagators of other PPs and hence the OCA equations also have to be solved self-consistently. Further details of the NCA and OCA impurity solver can be found, e.g., in Refs. 17, 31, and 42–45].

---

*djacob@mpi-halle.de

[1] J. J. Palacios, A. J. Pérez-Jiménez, E. Louis, and J. A. Vergés, Phys. Rev. B **64**, 115411 (2001).

[2] J. Taylor, H. Guo, and J. Wang, Phys. Rev. B **63**, 121104(R) (2001).

[3] N. Agraït, A. L. Yeyati, and J. M. van Ruitenbeek, Phys. Rep. **377**, 81 (2003), and references therein.

[4] M. Viret, S. Berger, M. Gabureac, F. Ott, D. Olligs, I. Petej, J. F. Gregg, C. Fermon, G. Francinet, and G. LeGoff, Phys. Rev. B **66**, 220401(R) (2002).

[5] C. Untiedt, D. M. T. Dekker, D. Djukic, and J. M. van Ruitenbeek, Phys. Rev. B **69**, 081401(R) (2004).

[6] Z. K. Keane, L. H. Yu, and D. Natelson, Appl. Phys. Lett. **88**, 062514 (2006).

[7] K. I. Bolotin, F. Kuemmeth, A. N. Pasupathy, and D. C. Ralph, Nano Lett. **6**, 123 (2006).

[8] D. Jacob, J. Fernández-Rossier, and J. J. Palacios, Phys. Rev. B **71**, 220403(R) (2005).

[9] A. Smogunov, A. DalCorso, and E. Tosatti, Phys. Rev. B **73**, 075418 (2006).

[10] J. Kondo, Prog. Theor. Phys. **32**, 37 (1964).

[11] M. R. Calvo, J. Fernández-Rossier, J. J. Palacios, D. Jacob, D. Natelson, and C. Untiedt, Nature (London) **458**, 1150 (2009).

[12] U. Fano, Phys. Rev. **124**, 1866 (1961).

[13] V. Madhavan, W. Chen, T. Jamneala, M. F. Crommie, and N. S. Wingreen, Science **280**, 567 (1998).

[14] L. Vitali, R. Ohmann, S. Stepanow, P. Gambardella, K. Tao, R. Huang, V. S. Stepanyuk, P. Bruno, and K. Kern, Phys. Rev. Lett. **101**, 216802 (2008).

[15] N. Néel, J. Kröger, R. Berndt, T. Wehling, A. Lichtenstein, and M. I. Katsnelson, Phys. Rev. Lett. **101**, 266803 (2008).

[16] N. Néel, J. Kröger, L. Limot, K. Palotas, W. A. Hofer, and R. Berndt, Phys. Rev. Lett. **98**, 016801 (2007).

[17] A. C. Hewson, *The Kondo Problem to Heavy Fermions* (Cambridge University Press, Cambridge, 1993).

[18] K. S. Thygesen and A. Rubio, J. Chem. Phys. **126**, 091101 (2007).

[19] A. Ferretti, A. Calzolari, R. Di Felice, F. Manghi, M. J. Caldas, M. Buongiorno Nardelli, and E. Molinari, Phys. Rev. Lett. **94**, 116802 (2005).

[20] D. Jacob, K. Haule, and G. Kotliar, Phys. Rev. Lett. **103**, 016803 (2009).

[21] P. Lucignano, R. Mazzarello, A. Smogunov, M. Fabrizio, and E. Tosatti, Nature Mater. **8**, 563 (2009).

[22] L. G. G. V. Dias da Silva, M. L. Tiago, S. E. Ulloa, F. A. Reboredo, and E. Dagotto, Phys. Rev. B **80**, 155443 (2009).

[23] D. Jacob and G. Kotliar, Phys. Rev. B **82**, 085423 (2010).

[24] A. Georges, G. Kotliar, W. Krauth, and M. J. Rozenberg, Rev. Mod. Phys. **68**, 13 (1996).

[25] D. Vollhardt, N. Blümer, K. Held, M. Kollar, J. Schlipf, and M. Ulmke, Z. Phys. B: Condens. Matter **103**, 283 (1997).

[26] V. Dobrosavljevic and G. Kotliar, Philos. Trans. R. Soc. London, Ser. A **356**, 57 (1998).

[27] M. Potthoff and W. Nolting, Phys. Rev. B **60**, 7834 (1999).

[28] S. Okamoto and A. J. Millis, Nature (London) **428**, 630 (2004).

[29] J. K. Freericks, *Transport in Multilayered Nanostructures: The Dynamical Mean-Field Theory Approach* (Imperial College Press, London, 2006).

[30] E. V. Gorelik, I. Titvinidze, W. Hofstetter, M. Snoek, and N. Blümer, Phys. Rev. Lett. **105**, 065301 (2010).

[31] G. Kotliar, S. Y. Savrasov, K. Haule, V. S. Oudovenko, O. Parcollet, and C. A. Marianetti, Rev. Mod. Phys. **78**, 865 (2006).

[32] K. Held, Adv. Phys. **56**, 829 (2007).

[33] D. Jacob, Ph.D. thesis, Universidad de Alicante, 2007.

[34] A. Valli, G. Sangiovanni, O. Gunnarsson, A. Toschi, and K. Held, Phys. Rev. Lett. **104**, 246402 (2010).

[35] S. Florens, Phys. Rev. Lett. **99**, 046402 (2007).

[36] R. Dovesi *et al.*, CRYSTAL06, Release 1.0.2, Theoretical Chemistry Group, Universita' Di Torino, Torino, Italy.

[37] A. Grechnev, I. DiMarco, M. I. Katsnelson, A. I. Lichtenstein, J. Wills, and O. Eriksson, Phys. Rev. B **76**, 035107 (2007).

[38] Here we use a minimal basis set plus effective core pseudopotential that takes into account the $4s$, $4p$, and $3d$ valence shells of the magnetic atoms (Ref. 55). $\mathbf{P}_d^{(i)}$ projects onto the Gaussian-type orbitals with d symmetry representing the $3d$ shell of the atom i.

[39] A. G. Petukhov, I. I. Mazin, L. Chioncel, and A. I. Lichtenstein, Phys. Rev. B **67**, 153106 (2003).

[40] Here we have orthogonalized the complete correlated subspace C composed of the $3d$ shells of all magnetic atoms which is treated within DMFT while the rest of the system is still nonorthogonal. Also in our treatment the correlated subspace C has overlap with the rest of the system. The use of nonorthogonal basis sets in the transport problem has been discussed, e.g., in Ref. 56.

[41] In the many-body and DMFT community, one would rather call Σ_L and Σ_R hybridization functions since they describe the dynamic hybridization of the device region with semi-infinite leads.

[42] N. E. Bickers, Rev. Mod. Phys. **59**, 845 (1987).

[43] T. Pruschke and N. Grewe, Z. Phys. B: Condens. Matter **74**, 439 (1989).

[44] K. Haule, S. Kirchner, J. Kroha, and P. Wölfle, Phys. Rev. B **64**, 155111 (2001).

[45] K. Haule, C.-H. Yee, and K. Kim, Phys. Rev. B **81**, 195107 (2010).

[46] Y. Meir and N. S. Wingreen, Phys. Rev. Lett. **68**, 2512 (1992).

[47] P. Werner, T. Oka, M. Eckstein, and A. J. Millis, Phys. Rev. B **81**, 035108 (2010).

[48] A. Dirks, P. Werner, M. Jarrell, and T. Pruschke, Phys. Rev. E **82**, 026701 (2010).

[49] R. Landauer, Philos. Mag. **21**, 863 (1970).

[50] D. Jacob, J. Fernández-Rossier, and J. J. Palacios, Phys. Rev. B **74**, 081402(R) (2006).

[51] D. Jacob, J. Fernández-Rossier, and J. J. Palacios, Phys. Rev. B **77**, 165412 (2008).

[52] K. S. Thygesen and A. Rubio, Phys. Rev. B **77**, 115333 (2008).

[53] C. Tard, X. Liu, S. K. Ibrahim, M. Bruschi, L. D. Gioia, S. C. Davies, X. Yang, L.-S. Wang, G. Sawers, and C. J. Pickett, Nature (London) **433**, 610 (2005).

[54] H. M. Pastawski and E. Medina, Rev. Mex. Fis. **47**, 1 (2001).

[55] M. M. Hurley, L. F. Pacios, P. A. Christiansen, R. B. Ross, and W. C. Ermler, J. Chem. Phys. **84**, 6840 (1986).

[56] K. S. Thygesen, Phys. Rev. B **73**, 035309 (2006).